



Frank T. Smith · Kevin Liu 

Three-dimensional evolution of body and fluid motion near a wall

Received: 15 December 2021 / Accepted: 3 October 2022 / Published online: 30 October 2022
© The Author(s) 2022

Abstract Evolution of three-dimensional body motion within surrounding three-dimensional fluid motion is addressed, each motion affecting the other significantly in a dynamic fluid–body interaction. This unsteady problem is set near a wall. The spatial three-dimensionality present is a new feature. For inviscid incompressible fluid, a basic nonlinear formulation is described, followed by a linearised form as a first exploration of parameter space and solution responses. The problem reduces to solving Poisson’s equation within the underbody planform, subject to mixed boundary conditions and to coupling with integral equations. Numerical and analytical properties show dependence mainly on the normal and pitch motions, as well as instability or bounded oscillations depending on the position of the centre of mass of the body, and a variety of three-dimensional shapes is examined.

Keywords Fluid–solid interactions · Three-dimensional · Near a wall · Poisson’s equation · Nonlinear and linearised formulation · Mixed boundary conditions · Numerical analysis

1 Introduction

A dynamic fluid–body interaction involves the unsteady motion of a solid body that is freely moving in a surrounding fluid and affecting the fluid flow substantially, which thereby affects the body motion substantially and produces two-way interplay. In the scenarios of current concern, we have an incident unidirectional fluid flow over a solid wall but with a free finite three-dimensional body located initially above the wall such that part of the oncoming fluid travels through the gap between the underneath of the body and the wall. This yields an unsteady three-dimensional interaction.

Background motivations for focussing on these interactions include the applications to industrial, biomedical and environmental modelling. Dynamic fluid–body interactions have been much studied through direct numerical simulations and experiments. Examples include contributions by Portela et al. [18], Wang and Levy [23], Dehgahan and Basir Tabrizi [3] concerned with turbulent flow and contributions by Hall [7], Einav and Lee [5], Petrie et al. (1993) [17], Schmidt and Young [19], Loisel et al. [13] on flow transition. Further related studies are by Owen [15], Miller et al. [14], Foucaut and Stanislas [6], Virmavirta et al. [22], Kudrolli et al. [11], Diplas et al. [4], Akoz and Kirkgoz [1], Hewitt et al. [8], Kudrolli et al. [12]. As far as we are aware, comparatively little analysis has ever been performed or presented in three spatial dimensions in the area despite the three-dimensionality of interactions in many practical configurations such as those above.

The works mentioned above are, to repeat, predominantly computational or experimental studies and much of the interest in those works as well as in the background motivations is centred on properties at fairly high

Communicated by Vassilios Theofilis.

Frank T. Smith (✉) · Kevin Liu
University College London, Gower Street, London WC1E 6BT, UK
E-mail: f.smith@ucl.ac.uk

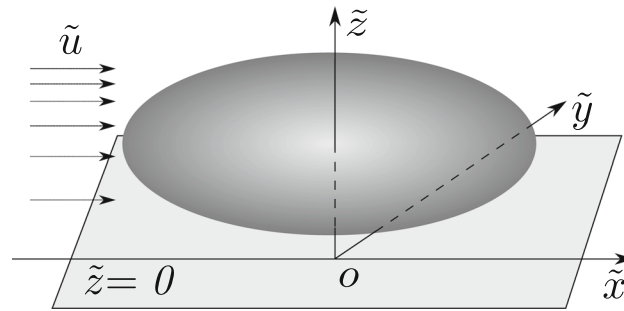


Fig. 1 Sketch (not to scale) of the three-dimensional body which is free to move in the otherwise uniform fluid flow, near a wall $\tilde{z} = 0$, leading to fluid–body interaction. Dimensional coordinates are shown

Reynolds numbers. In that parameter range relatively little exploration of fluid–body interaction has been undertaken even for two spatial dimensions in terms of applied mathematical studies apart perhaps from quite recent papers by Smith and Ellis [20], Smith and Wilson [21], Palmer and Smith [16], Jolley et al. [9] for inviscid fluids concerning bodies in boundary layers and channel flows. This sets the scene for the present study which is focussed on an applied mathematical investigation of a dynamic fluid–body interaction in three spatial dimensions.

The three-dimensional body is taken to be moving in the vicinity of the wall or ground and to be almost aligned with the wall. The body is thin as regards its representative dimension normal to the wall, relative to the typical streamwise and spanwise dimensions, and the spatial variation of the underbody shape is supposed to be of the same order as the thickness of the fluid-filled gap between the wall and the underbody. The fluid is assumed to be inviscid and incompressible and its motion to be laminar. There are connections here with the study in Jones and Smith [10] of three-dimensional flow due to a car underbody with ground effects present, but in the current cases the underbody is freely moving due to interaction with the fluid flow. The current scenario has the coordinate frame of reference to be used being such that the origin moves horizontally with the centre of mass of the body; the wall then appears as non-stationary in general. The oncoming fluid stream is assumed to be uniform.

Section 2 describes the formulation of the model, including the scales and the derivation of the unsteady three-dimensional system. See also Figs. 1, 2, 3. Here, the interaction in the gap between the underbody and the wall is found to exert most influence on the combined fluid and body motions. A model simplification with a linearised approach, in Sect. 3, is then adopted as a means of gaining a first appreciation of the parameter space involved. Section 4 describes analytical features and Sect. 5 discusses the numerical method which is applied to the system, while numerical case studies are presented in Sect. 6. Section 7 provides further discussion and conclusions.

2 Model formulation

The typical scales of \tilde{x} and \tilde{y} are comparable and can be denoted as \tilde{l} say, while the typical scale of \tilde{z} is \tilde{h} where the ratio $\tilde{h}/\tilde{l} \ll 1$. The body slopes are typically $O(\tilde{h}/\tilde{l})$. We therefore write, for the thin gap between the underbody and the wall,

$$(\tilde{x}, \tilde{y}, \tilde{z}) = \tilde{l}(X, Y, (\tilde{h}/\tilde{l})Z), \quad (1)$$

with X, Y, Z of order unity and anticipate that in the gap

$$(\tilde{u}, \tilde{v}, \tilde{w}) = \tilde{u}_\infty(U, V, (\tilde{h}/\tilde{l})W) + \dots, \quad (2a)$$

$$\tilde{p} = \rho_F \tilde{u}_\infty^2 P + \dots, \quad (2b)$$

$$\tilde{t} = (\beta \tilde{l}/\tilde{u}_\infty) T. \quad (2c)$$

Here, the expansions in (2a) follow from a balancing in the continuity equation as well as in the streamwise and spanwise momentum equations, the pressure expansion in (2b) is also inferred from those momentum balances; the positive constant β in the time scale (2c) is taken to be large, $\beta \gg 1$, which stems from the

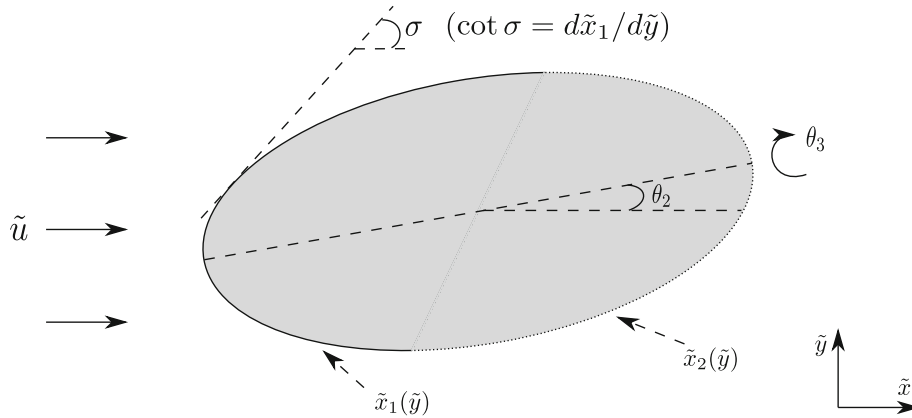


Fig. 2 A top-down plan view of the body in the (\tilde{x}, \tilde{y}) plane. The incoming stream \tilde{u} is aligned with the \tilde{x} -axis. The body's leading edge $\tilde{x}_1(\tilde{y})$ is depicted by a solid line, while the trailing edge $\tilde{x}_2(\tilde{y})$ is by a dotted line. The angle of rotation about the \tilde{z} -axis (yaw) is denoted as θ_2 , and θ_3 denotes the rotation about the \tilde{x} -axis (roll). σ is the angle between the tangent to the leading edge $\tilde{x}'_1(\tilde{y})$ and the outer stream direction (\tilde{x} -axis)

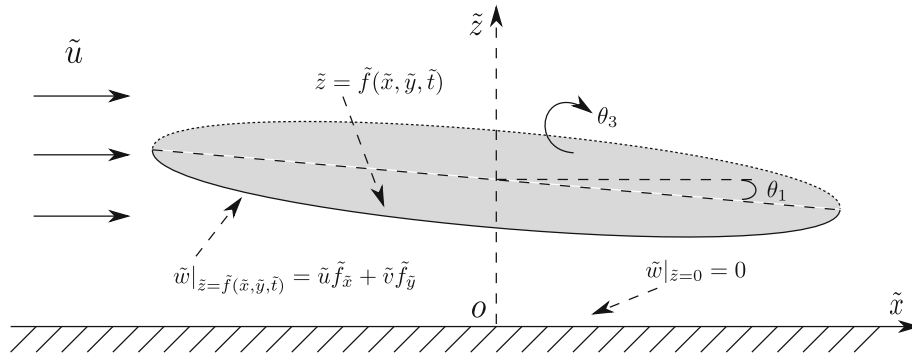


Fig. 3 A cross-sectional view of the body in the (\tilde{x}, \tilde{z}) plane. The incoming stream \tilde{u} is aligned with the \tilde{x} -axis. The under-body surface is denoted by $\tilde{f}(\tilde{x}, \tilde{y}, \tilde{t})$; the kinematic conditions for \tilde{w} at $\tilde{z} = \tilde{f}$ and $\tilde{z} = 0$ are illustrated in the diagram. The angle of rotation about the \tilde{y} -axis (pitch) is denoted as θ_1 , and θ_3 denotes the rotation about the \tilde{x} -axis (roll)

property that for a sufficiently dense body the representative time scale of the body motion is significantly greater than that of the fluid motion.

The fluid motion in the thin gap is then governed by a nonlinear thin-layer system in 3D for an inviscid fluid, namely the continuity equation and two momentum equations in X, Y of the form

$$U_X + V_Y + W_Z = 0, \tag{3a}$$

$$UU_X + VU_Y + WU_Z = -P_X, \tag{3b}$$

$$UV_X + VV_Y + WV_Z = -P_Y. \tag{3c}$$

The order unity scaled pressure $P = P(X, Y, T)$ here is independent of the normal coordinate Z by virtue of the normal momentum balance. The boundary conditions below are written now for a leading edge planform of body with shape which is given in general by $X = X_1(Y)$, and F denotes the body surface in contact with the fluid:

$$W|_{Z=0} = 0, \tag{4a}$$

$$W|_{Z=F(X,Y,T)} = UF_X + VF_Y, \tag{4b}$$

$$(U, V, W, P) = (1, 0, 0, 0), \quad (\text{in the incoming stream}), \tag{4c}$$

$$U \cos \sigma + V \sin \sigma = \cos \sigma, \quad (\text{at inflow edges } X = X_1(Y)+), \tag{4d}$$

$$P = 0, \quad (\text{at trailing edges } X = X_2(Y)-). \tag{4e}$$

The condition (4a) corresponds to the requirement of tangential flow at the solid wall and the condition (4b) is the kinematic condition at the moving underbody surface F ; we repeat that the scaled time T is slow in terms of the fluid flow. Further, (4c) represents the match with the oncoming flow in the far field and (4d) refers to the expected continuous quantities, but there are also discontinuities in velocity and pressure across the leading edge of the planform as $X \rightarrow X_1^-$ and $X \rightarrow X_1^+$. Here, σ is the angle between the tangent to the curved leading edge and the outer stream direction (X -axis), such that $\cot \sigma = X_1'(Y)$ [10]. The condition (4d) stems from a thin Euler-like region lying along the leading edge in which the horizontal velocity component normal to the edge adjusts in a quasi-planar manner along with the vertical velocity; the distance coordinate, s , along the edge being of order unity but the tangential component is convected pressure-free along the inward directed streamlines locally. Consequently, the horizontal velocity tangential to this edge is continuous across the above region. In (4d) moreover, U, V are expected to be independent of Z , although usually they depend on s . Constraint (4e) is associated with the Kutta-like requirement that the pressure be continuous across the trailing edge of the planform [10,20]. This last condition leads to the constraint that P must be zero for any trailing edge location at the boundary of the planform, the reason being that the thinness of the body induces only small variations in P except in the gap where P is of order unity. We comment also that as in the 2D case [20,21] there is upstream influence present in spite of the locally parabolic nature of the governing equations (3). The leading edge here corresponds to fluid particles which travel from the surrounding flow onto or beneath the body, whereas the trailing edge refers to particles travelling into the surrounding flow. In the present nonlinear setting, the junctions between the leading and trailing edges are unknown in advance.

The body motion is now considered. Dynamic fluid–body interaction occurs when the body is free to move, its motion being controlled by the forces and moments due to the flow pressure. In the present configuration of a thin body, only three factors are directly interactive with the motion, over the current time scales, namely the scaled lift force L_Z acting in the normal direction, the scaled moment or torque M_Y acting about the Y -axis and the scaled moment M_X about the X -axis. The corresponding drag force L_X in the X direction, for instance, is too small to alter the streamwise movements, which consist of the body continuing to translate at its initial velocity (thus, relative to the body, the oncoming stream is uniform as in (4c)), and similarly the spanwise drag force L_Y in the Y direction and the moment M_Z about the Z -axis are negligible. The translational velocities $U = 1, V = 0$ in the streamwise and spanwise directions are therefore uniform and likewise for any angular velocity $d\theta/dT$ about the Z -axis. On the other hand, the flow pressure is dependent on the body shaping as is evident from the original problem (3-4). So the fluid and body motions are coupled.

The scaled angles of rotation about the Y, Z, X axes are written $\Theta_1(T), \Theta_2(T), \Theta_3(T)$, denoting the pitch, yaw and roll angles, respectively; the vertical distance moved by the body is $H(T)$ and X_c, Y_c denote the X -wise and Y -wise centres of mass in turn. The rates of change of X_c, Y_c and the yaw angle Θ_3 are taken to be zero as a prime example. We have

$$m \frac{d^2 H}{dT^2} = \iint P(X, Y, T) dX dY, \quad (5a)$$

$$j_1 \frac{d^2 \Theta_1}{dT^2} = \iint (X - X_c) P(X, Y, T) dX dY, \quad (5b)$$

$$j_2 \frac{d^2 \Theta_2}{dT^2} = \iint (Y - Y_c) P(X, Y, T) dX dY, \quad (5c)$$

where the double integrals extend over the XY -planform of the body. Here, m, j_1, j_2 are, respectively, the scaled mass and moments of inertia with respect to Θ_1, Θ_2 . Also the leading edge X_1 and trailing edge X_2 are quasi-steady, as is the fluid flow, in contrast with the motion of the body which is fully unsteady with scaled time variable T of order unity. The underbody shape is given by

$$F(X, Y, T) = G(X, Y) + H(T) + (X - X_c)\Theta_1(T) + (Y - Y_c)\Theta_2(T). \quad (6)$$

The largeness of the factor β mentioned after (2c) is consistent with the body-motion balances in (5), provided that the density ratio ρ_B/ρ_F is sufficiently large.

3 Model simplifications and linearised interactions

Returning to the fluid dynamical part of the model, we seek a solution in which U, V are uniform in Z inside the gap. The conditions (4a, 4b) then establish that the velocity components must satisfy

$$\frac{\partial(UF)}{\partial X} + \frac{\partial(VF)}{\partial Y} = 0, \tag{7}$$

while (3b, 3c) with (4c) imply that the vertical vorticity is zero, leading to the forms $U = \partial\Phi/\partial X, V = \partial\Phi/\partial Y$. Here, $\Phi(X, Y, T)$ is the scaled vertical potential function, it is governed by the elliptic equation

$$\frac{\partial}{\partial X} \left(F \frac{\partial\Phi}{\partial X} \right) + \frac{\partial}{\partial Y} \left(F \frac{\partial\Phi}{\partial Y} \right) = 0, \tag{8}$$

on account of (7), with the pressure then given by

$$P = \frac{1}{2} \left(1 - \left(\frac{\partial\Phi}{\partial X} \right)^2 - \left(\frac{\partial\Phi}{\partial Y} \right)^2 \right). \tag{9}$$

The planform-edge boundary conditions (4d, 4e) written in terms of Φ thus become

$$\Phi = X, \tag{at } X = X_1(Y)), \tag{10a}$$

$$\text{align} \left(\frac{\partial\Phi}{\partial X} \right)^2 + \left(\frac{\partial\Phi}{\partial Y} \right)^2 = 1, \tag{at } X = X_2(Y)). \tag{10b}$$

The fluid flow is thus controlled by (8-10) but with the unknown moving shape $F(X, Y, T)$ in (8) coupling the fluid flow with the body motion through (5-6).

Some ideas on solving the fluid-flow part (8-10) alone are presented in Sect. 5.2 of Jones and Smith [10], especially equations (5.4)–(5.6) there. The presence of the body-motion part (5-6) in the current overall system makes it more difficult however. So we turn to an analytical investigation next.

A linearised version of the problem described in the previous section is found to yield valuable insight. We write:

$$(X, Y, Z, T) \sim (x, y, z, t), \tag{11a}$$

$$(F - 1, H, G, \Theta_1, \Theta_2) \sim \epsilon(f, h, g, \theta_1, \theta_2). \tag{11b}$$

For this almost-constant case $F = 1 + \epsilon f$ with the parameter ϵ being small, we can perform a linearisation such that the potential function Φ and pressure P expand as

$$\Phi = x + \epsilon\phi(x, y, t) + O(\epsilon^2), \tag{12a}$$

$$P = 0 + \epsilon p + O(\epsilon^2). \tag{12b}$$

Substitution into (8) shows that at leading order we are then left with solving

$$\frac{\partial^2\phi}{\partial x^2} + \frac{\partial^2\phi}{\partial y^2} = -\frac{\partial f}{\partial x}, \tag{13}$$

for the perturbation potential $\phi(x, y, t)$. The boundary conditions at the given planform edge of the body are now

$$\phi = 0, \tag{at } x = x_1(y)), \tag{14a}$$

$$\frac{\partial\phi}{\partial x} = 0, \tag{at } x = x_2(y)) \tag{14b}$$

from (10). For prescribed underbody $f(x, y, t)$ and planform shape the formulation (13)-(14) constitutes a closed problem for $\phi(x, y, t)$, once ϕ is found then the pressure p follows from

$$p(x, y, t) = -\frac{\partial\phi}{\partial x}. \tag{15}$$

Further, the rates of change of x_c , y_c and the yaw angle θ_3 referred to in the previous section are taken to be zero as a prime example. It is notable also that the junctions between inflow and outflow edges (leading and trailing edges) are known in advance for the current linearised setting.

The underbody shape perturbation is given, from (6), by

$$f(x, y, t) = g(x, y) + h(t) + (x - x_c)\theta_1(t) + (y - y_c)\theta_2(t), \quad (16)$$

and coupled with the above we have, from (5):

$$m \frac{d^2 h}{dt^2} = \iint p(x, y, t) dx dy, \quad (17a)$$

$$j_1 \frac{d^2 \theta_1}{dt^2} = \iint (x - x_c) p(x, y, t) dx dy, \quad (17b)$$

$$j_2 \frac{d^2 \theta_2}{dt^2} = \iint (y - y_c) p(x, y, t) dx dy, \quad (17c)$$

where, to repeat, the double integrals are over the xy -planform of the body. The governing equations and boundary conditions of the interaction are now thus (13-17); initial conditions on h , θ_1 , θ_2 and their temporal derivatives h' , θ_1' , θ_2' are assumed known at time zero.

Concerning solution properties, first we see that the roll angle θ_2 has no effect on the total interaction. This is a perhaps surprising feature. It happens because, in (16), θ_2 contributes to f only a term independent of x and has no influence on ϕ due to the right-hand side of (13), and hence no influence on pressure p and no influence on the double-integral forces in (17). Therefore, the body's roll angle is able to evolve simply as $\theta_2(0) + \theta_2'(0)t$ (where the constants are determined by the initial conditions), giving a uniform rolling movement of the body. This makes physical sense since the rolling takes place in a plane perpendicular to the oncoming stream. Second, it is similarly clear that the body's vertical displacement $h(t)$ in (16) has no effect on the evolution of the pitch angle $\theta_1(t)$ by virtue of the x -derivative on the right-hand side of (13). Hence, the linearised interaction reduces to (13-17b) in effect. Third, a numerical treatment of this linearised interaction is called for in general, following the analysis immediately below.

4 Analysis of special model cases

This section provides analytical features of several special model shapes, which can serve as helpful comparisons for the numerical work to be discussed in the next section, as well as shedding some extra light on the overall solution properties. The special cases considered here are (a) the circular planform, (b) the almost 2D case associated with a large span in the y direction and (c) the thin-planform case of a relatively small span in the y direction.

4.1 On the circular planform when g is negligible

This corresponds to the special case where $f = \theta_1 x$ (which is also concerned with exponential growth, see below), whose visual illustration is given in Fig. 4a. The basic problem in the real plane is then to solve the Poisson equation

$$\Delta \phi = -\theta_1 \quad (18)$$

inside the semi-circle bounded by $r = 1$ and $y = 0$, together with the boundary conditions

$$\phi = 0, \quad \left(\text{at } r = 1, \frac{\pi}{2} < \theta < \pi \right), \quad (19a)$$

$$\frac{\partial \phi}{\partial x} = 0, \quad \left(\text{at } r = 1, 0 < \theta < \frac{\pi}{2} \right), \quad (19b)$$

$$\frac{\partial \phi}{\partial y} = 0, \quad \left(\text{at } y = 0, -1 < x < 1 \right). \quad (19c)$$

In this subsection, we are working for convenience in terms of $x = r \cos \theta$, $y = r \sin \theta$ as the planar Cartesian coordinates and $\omega = x + iy$ is the associated complex coordinate. The condition (19c) stems from symmetry about the x -axis in the original circle case. The analytical solution via conformal mapping can be found in ‘‘Appendix 7’’, where the pressure along the boundary of the flow domain is obtained and shown in Fig. 4. The result is found to agree closely with the direct numerical solution of this special case.

4.2 On the nearly-2D case

Here, the parameter q is large; $|y|$ is large compared with $|x|$ and the y derivatives become relatively small. With leading and trailing edge positions written suitably as $x = x_1(y)$, $x = x_2(y)$, respectively, equation (13) for the special case $f = \theta_1 x$ (see Fig. 5c) gives us

$$\frac{1}{\theta_1} \frac{\partial^2 \phi}{\partial x^2} = -1 \tag{20}$$

to leading order and so since we require $\phi = 0$ at $x = x_1$ and $\partial\phi/\partial x = 0$ at $x = x_2$ we have

$$\frac{\phi}{\theta_1} = \left[-\frac{1}{2}(x - x_1)^2 + (x_2 - x_1)(x - x_1)\right]. \tag{21}$$

Hence, the pressure solution is simply

$$\frac{P}{\theta_1} = x - x_2. \tag{22}$$

The torque τ is, therefore, the integral from x_1 to x_2 of $(x - x_c)p$ with respect to x , giving

$$\frac{\tau}{\theta_1} = \frac{1}{2} (x_2 - x_1)^2 \left(x_c - x_1 - \frac{x_2 - x_1}{3}\right). \tag{23}$$

Here, $B_1 = B - A$ and $C_1 = c - A$. Consequently, we see that τ/θ_1 is negative for $(x_c - x_1) < (x_2 - x_1)/3$ and positive for $x_c - x_1 > (x_2 - x_1)/3$. The tipping point is thus 1/3 of the distance from the leading edge to the trailing edge. Because of (17b), a CoM (centre of mass) lying ahead of the tipping point leads to oscillations of θ_1 and a CoM behind the tipping point leads to exponential growth.

Figure 5 demonstrates the contrasting behaviours of the body motion for different centre of mass positions $x_c = -1$ and 0; the body is configured to have a large span along the y -axis with $q = 10$ in (30), as such the flow domain is of an ellipse with $x \in [-1, 1]$, $y \in [-10, 10]$. Figure 5a–b shows the oscillatory behaviour of the body’s pitch angle θ_1 and height h when its centre of mass is at the leading edge $x_c = -1$, whereas Figure 5c–d shows the exponential growth nature of θ_1 and h when $x_c = 0$ and is behind the 1/3 threshold.

4.3 On the very thin case

This is for $q \ll 1$ in the ellipse notation where the y scale \ll the x scale. So the governing equation (13) becomes

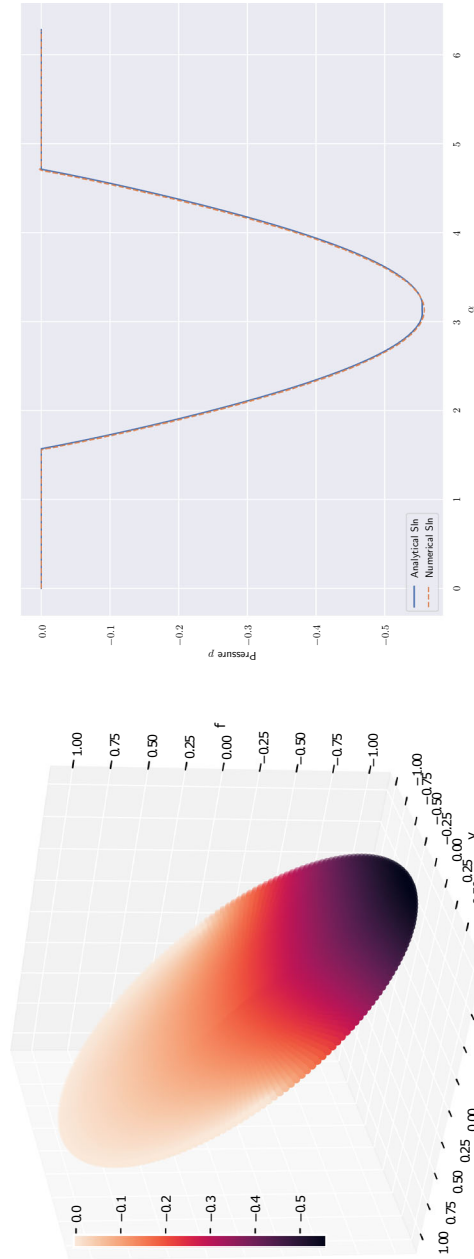
$$\frac{\partial^2 \phi}{\partial y^2} = -\frac{\partial f}{\partial x} \tag{24}$$

to leading order. If the body surface function f is independent of y throughout then we obtain, for $x < 0$,

$$\phi = \frac{1}{2} (\Omega(x)^2 - y^2) \frac{\partial f}{\partial x} \tag{25}$$

after applying the conditions that $\phi = 0$ at the planform edges which are given by $y = \Omega(x)$ and $y = -\Omega(x)$ say. The pressure here is therefore

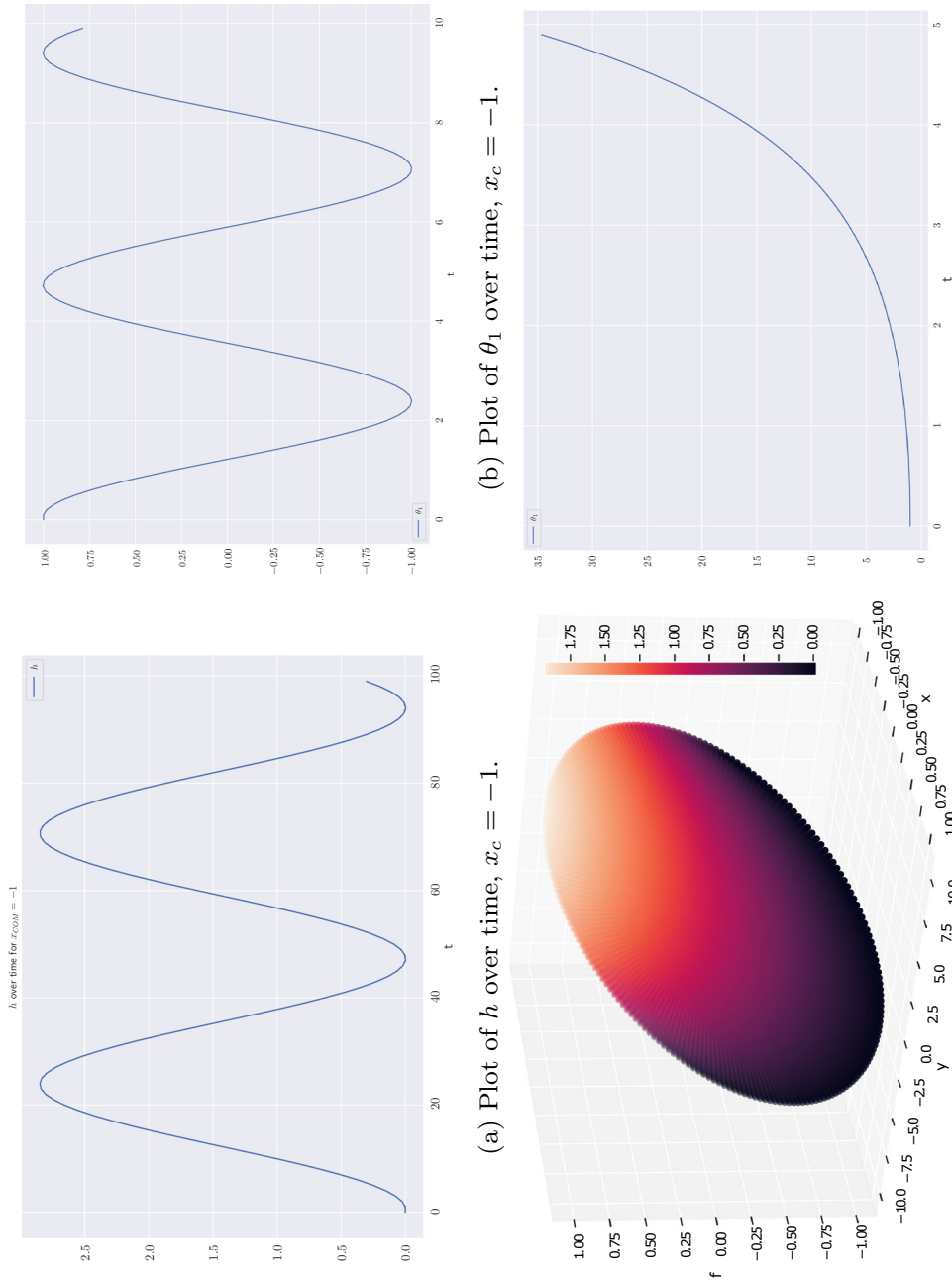
$$P = P^- = \frac{1}{2} \left(y^2 \frac{\partial^2 f}{\partial x^2} - \frac{\partial}{\partial x} \left(\Omega^2 \frac{\partial f}{\partial x} \right) \right). \tag{26}$$



(a) Plot of the circular body ($q = 1$) whose under body height function is given as $f = x$; the colouring represents a heat map for the pressure exerted on the body's surface.

(b) Plot of numerical and conformal mapping pressure solutions (the graphs are almost identical) along the outer boundary of the body flow domain. Note its correspondence with the pressure heat map given in Fig 4a.

Fig. 4 Comparison of conformal mapping versus numerical solution of the pressure along the boundary of the circular flow domain $q = 1$, with the body shape given as $f = \theta_1 x$ where $\theta_1 = 1$



(c) Plot of the body surface and its pressure heat map.

(d) Plot of θ_1 over time, $x_c = 0$.

Fig. 5 Evolution of the pitch angle θ_1 and body height h for different centres of mass configurations of a body with large span along the y -axis. The body surface function is given as $f = \theta_1 x$, with the initial values of θ_1 and h taken to be -1 and 0 , respectively

For $x > 0$ application of the requirement $\partial\phi/\partial x = 0$ at the edges leads to the pressure being

$$P = P^+ = \frac{1}{2}(y^2 - \Omega^2) \frac{\partial^2 f}{\partial x^2}. \quad (27)$$

In the special case of $f = \theta_1 x$, these pressures reduce to: $P^- = -\theta_1 \Omega \Omega_x$, $P^+ = 0$. Thus, when the scaled angle θ_1 is positive the scaled pressure is negative under the front half of the body but zero under the rear half. Additionally for the example of the ellipse where $(x/A)^2 + (y/B)^2 = 1$, thus $\Omega(x) = B(1 - x^2/A^2)^{\frac{1}{2}}$, we have in the special case that

$$P^- = \theta_1 (B/A)^2 x, \quad (-A < x < 0), \quad (28a)$$

$$P^+ = 0, \quad (0 < x < A). \quad (28b)$$

The torque τ follows from (5) as:

$$\tau = \frac{B^2}{6} \theta_1 (2A + 3x_c). \quad (29)$$

This implies that the critical position of the centre of mass, say x_k , takes the value $x_k = -2A/3$, corresponding to criticality at 1/6 of the chord measured from the leading edge of the planform. If $x_c < x_k$ then τ/θ_1 is negative from (6) and so the angular momentum equation (A7) yields $(d^2\theta_1/dt^2)/\theta_1$ being negative, implying oscillatory behaviour. If $x_c > x_k$ on the other hand then exponential growth is implied. Such behaviour can be seen in our direct numerical solutions in Fig. 6; we also demonstrate the agreement in pressure solution implied in (28) in Fig. 6b.

5 Numerical methods

Here, we present a numerical method of solving the Poisson equation with mixed boundary conditions in (13, 14), which involves at each time step encoding their finite difference discretisations as coefficients of a sparse linear equation matrix. So long as our model is well posed and correctly discretised, this encoding matrix should be well conditioned and invertible, and its solution yields our desired flow potential over the discretisation grid. This method can be repeated and marched forward in time to obtain the body's motion.

We begin by establishing the shape of the flow channel. Suppose the vertical projection of the body onto the ground is in the shape of an ellipse, which can be configured as a reasonable approximation to a wide range of model objects. The flow gap of interest is the space between this ground area and the lower surface of the body. The lower body's surface need not be smooth, instead it can have various "bumps" and "grooves" prescribed via the underbody surface function (16); various surface configurations will be demonstrated as part of our solution analysis.

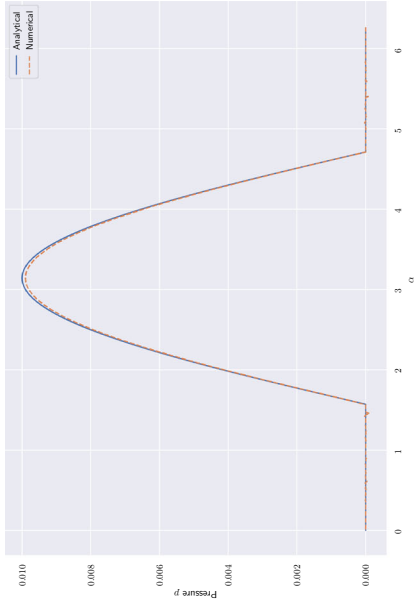
Since the 3D flow problem is reduced to characteristically 2D as outlined in Sect. 3's linearisation analysis and has a domain of elliptical shape, we first translate the model equations into elliptical coordinates before applying any numerical treatments. Suppose the flow domain centred at the origin is given by $x^2/A^2 + y^2/B^2 = 1$, where $2A$ and $2B$ are the lengths of the ellipse's two axes, or equivalently:

$$x^2 + \frac{1}{q^2} y^2 = A^2, \quad (30)$$

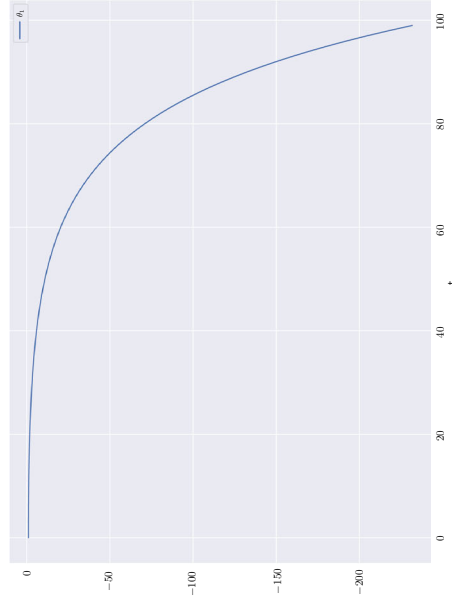
where $q = B/A$; the parameter q is a constant and prescribed based on the model shape. In elliptical coordinates, we write $x = r \cos(\theta)$ and $y = qr \sin(\theta)$ for $r \in (0, A]$ and $\theta \in (0, 2\pi]$; thus, the Poisson model equation (13) becomes:

$$\begin{aligned} & (\cos^2 \theta + q^{-2} \sin^2 \theta) \frac{\partial^2 \phi}{\partial r^2} + r^{-2} (\sin^2 \theta + q^{-2} \cos^2 \theta) \frac{\partial^2 \phi}{\partial \theta^2} + r^{-2} (1 - q^{-2}) \sin 2\theta \frac{\partial \phi}{\partial \theta} \\ & + r^{-1} (\sin^2 \theta + q^{-2} \cos^2 \theta) \frac{\partial \phi}{\partial r} - r^{-1} (1 - q^{-2}) \sin 2\theta \frac{\partial^2 \phi}{\partial \theta \partial r} = \frac{\sin \theta}{r} \frac{\partial f}{\partial \theta} - \cos \theta \frac{\partial f}{\partial r}. \end{aligned} \quad (31)$$

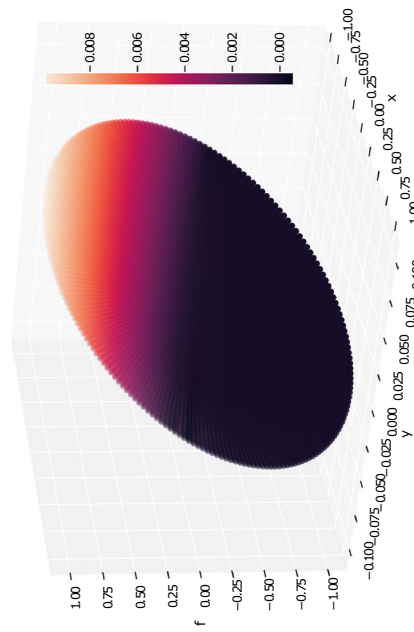
Now introducing the finite difference scheme, we take A to be unity without loss of generality and impose a $M \times N$ discretisation grid over this elliptical domain such that $M\Delta r = 1$, $N\Delta\theta = 2\pi$, where $r = i\Delta r$,



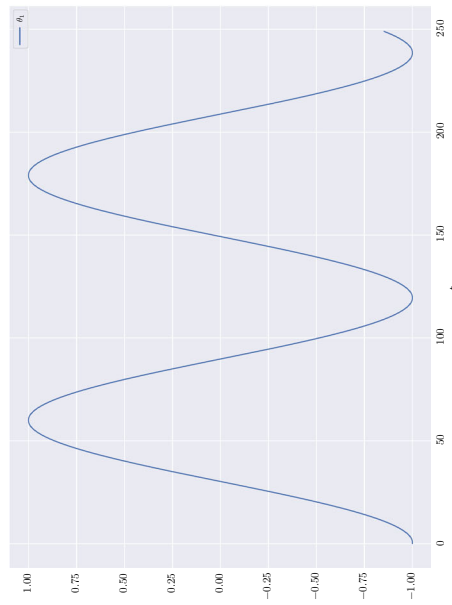
(b) Numerical and conformal mapping pressure solution at the body boundary, $x_c = 0$.



(d) Evolution of pitch angle θ_1 for a body with $x_c = 0$. The solution exhibits an exponential growth behaviour as $x_c > 1/6$ cord.



(a) Plot of the elliptical body ($q = 0.1$) and its pressure heat map.



(c) Evolution of pitch angle θ_1 for a body with $x_c = -1$. The solution exhibits the oscillatory behaviour as $x_c < 1/6$ cord.

Fig. 6 Various solutions of the planning model over an elliptical flow domain where $q = 0.1$; the body shape given as $f = -(x - x_c)$

$\theta = j\Delta\theta$ and $i \in [1, M]$, $j \in [1, N]$. Note our grid points do not include the origin itself where $r = 0$. The discretised Poisson equation (31) will be treated in three separate sections:

- 1) on the exterior curve $r = 1$, where the boundary conditions (14) apply;
- 2) on the innermost curve surrounding the origin, $r = \Delta r$;
- 3) in the interior enclosed by the innermost curve and the outer boundary.

On the interior section where $i \in [2, M - 1]$ and $j \in [1, N]$, the Poisson equation (31) can be discretised using a 4th-order central finite difference scheme:

$$\begin{aligned} & (C_1^j + \frac{C_2^j}{2i})\phi_{i+1,j} + (C_1^j - \frac{C_2^j}{2i})\phi_{i-1,j} - 2(C_1^j + \frac{C_2^j}{i^2\Delta\theta^2})\phi_{i,j} + (\frac{C_2^j}{i^2\Delta\theta^2} + \frac{C_3^j}{2i^2})\phi_{i,j+1} + (\frac{C_2^j}{i^2\Delta\theta^2} \\ & - \frac{C_3^j}{2i^2})\phi_{i,j-1} - \frac{C_3^j}{4i}(\phi_{i+1,j+1} - \phi_{i+1,j-1} - \phi_{i-1,j+1} + \phi_{i-1,j-1}) = \Delta r^2(\frac{\sin\theta}{r}\frac{\partial f}{\partial\theta} - \cos\theta\frac{\partial f}{\partial r}), \end{aligned} \tag{32}$$

where $C_1^j = \cos^2(j\Delta\theta) + q^{-2}\sin^2(j\Delta\theta)$, $C_2^j = \sin^2(j\Delta\theta) + q^{-2}\cos^2(j\Delta\theta)$ and $C_3^j = (1 - q^{-2})\Delta\theta^{-1}\sin(2j\Delta\theta)$. We leave the Right-Hand-Side (R.H.S.) of the equation undiscretised for presentation simplicity: a body surface function f can be discretised using an appropriate finite difference scheme or, in many cases, its derivatives are explicitly known. Since there are in total $M \times N$ grid points and thus as many unknown fluid potential data points, this ‘‘interior discretisation’’ offers $(M - 2) \times N$ linear equations with unknowns of $\phi_{i,j}$ for $i \in [2, M - 1]$, $j \in [1, N]$.

On the exterior boundary, there are two boundary conditions. Firstly at $a = 1$ and $\theta \in [\frac{\pi}{2}, \frac{3\pi}{2}]$, we have the Dirichlet condition:

$$\phi_{M,j} = 0, \tag{33}$$

secondly on the rest of the curve we have the Neumann condition for $\theta \in (-\frac{\pi}{2}, \frac{\pi}{2})$:

$$\frac{\partial\phi}{\partial x} = \cos\theta\frac{\partial\phi}{\partial r} - \sin\theta\frac{\partial\phi}{\partial\theta} = 0,$$

which can be discretised using a 4-th order backward difference scheme:

$$\begin{aligned} & \cos(j\Delta\theta)(\frac{25}{12}\phi_{M,j} - 4\psi_{M-1,j} + 3\psi_{M-2,j} - \frac{4}{3}\phi_{M-3,j} + \frac{1}{4}\phi_{M-4,j}) \\ & - \frac{\sin(j\Delta\theta)}{M\Delta\theta}(\frac{1}{12}\phi_{M,j-2} - \frac{2}{3}\phi_{M,j-1} + \frac{2}{3}\phi_{M,j+1} - \frac{1}{12}\phi_{M,j+2}) = 0. \end{aligned} \tag{34}$$

These two boundary conditions together offer another N linear equations for the unknowns of $\phi_{M,j}$ for $j \in [1, N]$.

Finally, to discretise the innermost curve we find an approximation to the fluid potential at the origin $\phi_{0,j}$, which itself is off the discretisation grid. To do so we apply a Taylor expansion of the fluid potential at $r = 0$:

$$\phi_{1,j} = \phi_{0,j} + \Delta r\frac{\partial\phi}{\partial r}(0,j) + \frac{1}{2}\Delta r^2\frac{\partial^2\phi}{\partial r^2}(0,j) + O(\Delta r^3). \tag{35}$$

Note that we opted to write the fluid potential at the origin as $\phi_{0,j}$ as opposed to ϕ_0 ; this should be the same value for all angle indexes j at this point of origin (at least in theory). We do so to keep track of the discretisation angle as will become clear below. The first-order derivative $\frac{\partial\phi}{\partial r}(0,j)$ can be discretised via a central difference scheme as:

$$\frac{\partial\phi}{\partial r}(0,j) = \frac{2}{3}(\phi_{1,j} - \phi_{1,\bar{j}}) - \frac{1}{12}(\phi_{2,j} - \phi_{2,\bar{j}}),$$

where $\bar{\theta} = \bar{j}\Delta\theta$ is the 180° reflection of the angle $\theta = j\Delta\theta$ over the point of origin, that is $\bar{\theta} = |\theta + \pi, 2\pi|$; likewise for the second-order derivative $\frac{\partial^2\phi}{\partial r^2}(0,j)$:

$$\frac{\partial^2\phi}{\partial r^2}(0,j) = -\frac{5}{2}\phi_{0,j} + \frac{4}{3}(\phi_{1,j} + \phi_{1,\bar{j}}) - \frac{1}{12}(\phi_{2,j} + \phi_{2,\bar{j}}).$$

Substituting the two expressions into Taylor expansions of (35) gives the following discretisation of the fluid potential at the point of origin:

$$\phi_{0,j} = \frac{4}{3}\phi_{1,j} - \frac{1}{2}\phi_{2,j} + \frac{1}{6}\phi_{2,\bar{j}}. \tag{36}$$

We now can discretise the Poisson equation on the innermost curve via a central difference scheme. Substituting in the origin discretisation of (36) where necessary we have all the grid points we need to apply our scheme:

$$\begin{aligned} &\frac{2C_1^j + 3C_2^j}{4}\phi_{2,j} + \frac{2C_1^j - C_2^j}{12}\phi_{2,\bar{j}} + \frac{C_3^j}{24}(\phi_{2,\bar{j}+1} - \phi_{2,\bar{j}-1}) - \frac{3C_3^j}{8}(\phi_{2,j+1} - \phi_{2,j-1}) - \left(\frac{5C_3^j}{6} \right. \\ &\left. - \frac{C_2^j}{\Delta\theta^2}\right)\phi_{1,j-1} - \frac{2}{3}\left(C_1^j + \frac{3 + \Delta\theta^2}{\Delta\theta^2}C_2^j\right)\phi_{1,j} + \left(\frac{5C_3^j}{6} + \frac{C_2^j}{\Delta\theta^2}\right)\phi_{1,j+1} = \Delta r^2\left(\frac{\sin\theta}{r}\frac{\partial f}{\partial\theta} - \cos\theta\frac{\partial f}{\partial r}\right). \end{aligned} \tag{37}$$

This, therefore, delivers another set of N equations for $\phi_{1,j}$ for $j \in [1, N]$, and we thus have altogether $M \times N$ linear equations for the same number of unknowns $\phi_{i,j}$.

To solve this finite difference system, we encode the equations of (32, 33, 34, 36) into a $(M \times N) \times (M \times N)$ linear equation system:

$$\begin{aligned} &\begin{bmatrix} -\frac{2}{3}(C_1^1 + \frac{3+\Delta\theta^2}{\Delta\theta^2}C_2^1), & \frac{5C_3^1}{6} + \frac{C_2^1}{\Delta\theta^2}, & 0, & \dots & 0 \\ -(\frac{5C_3^2}{6} - \frac{C_2^2}{\Delta\theta^2}), & -\frac{2}{3}(C_1^2 + \frac{3+\Delta\theta^2}{\Delta\theta^2}C_2^2), & \frac{5C_3^2}{6} + \frac{C_2^2}{\Delta\theta^2}, & \dots & 0 \\ \vdots & \vdots & \vdots & \dots & \vdots \\ \vdots & \vdots & \vdots & \dots & \vdots \\ \vdots & \vdots & \vdots & \dots & \vdots \\ 0, & 0, & 0, & \dots & \frac{25}{12}\cos((N-1)\Delta\theta) \\ 0, & 0, & 0, & \dots & \frac{25}{12}\cos(N\Delta\theta) \end{bmatrix} \begin{bmatrix} \phi_{1,1} \\ \phi_{1,2} \\ \vdots \\ \vdots \\ \phi_{M,N-1} \\ \phi_{M,N} \end{bmatrix} \\ &= \begin{bmatrix} -\Delta r^2 \frac{\partial f}{\partial x} \Big|_{1,1} \\ -\Delta r^2 \frac{\partial f}{\partial x} \Big|_{1,2} \\ \vdots \\ \vdots \\ 0 \\ 0 \end{bmatrix}. \end{aligned} \tag{38}$$

This sparse matrix, which consists of $M \times N$ linearly independent equations, is of full rank and invertible: it can be solved using a linear algebra software package such as NeRSC’s SuperLU. At each time step, we solve this linear system of fluid potentials ϕ , based on which the pressure p can be deduced via (15), and we subsequently obtain the body’s positional parameters h , θ_1 and θ_2 through (17), where the double integrals are evaluated via the composite trapezoidal rule. This scheme can be repeated and marched forward in time to obtain the combined evolution of the body and fluid motions.

Figure 7 demonstrates this numerical solver over a circular domain for a test case where the fluid potential is $\phi = r^2(\sin\theta + \cos\theta)$ and $r \in (0, 1]$. In this test case, $q = 1$ in equation (30) and the left-hand-side of equation (31) becomes $3r^2(\sin\theta + \cos\theta)$; consequently, the Dirichlet and Neumann conditions become $\phi = \sin\theta + \cos\theta$ and $\cos\theta\frac{\partial\phi}{\partial r} - \frac{\sin\theta}{r}\frac{\partial\phi}{\partial\theta} = \sin\theta\cos\theta + \cos^2\theta + 1$, respectively. The test case shows the solution of our numerical solver agrees with the real solution closely.

6 Numerical case studies

In this section, we apply the aforementioned numerical scheme to bodies with various shapes, particularly by adding a “thickness” function $g(x, y)$ to the body shape f , i.e. $f(x, y, t) = g(x, y) + x\theta_1(t)$. We assume the body’s centre of mass is at the origin throughout this section and $\theta_1(t)$ is the angle that controls the pitch of the body.

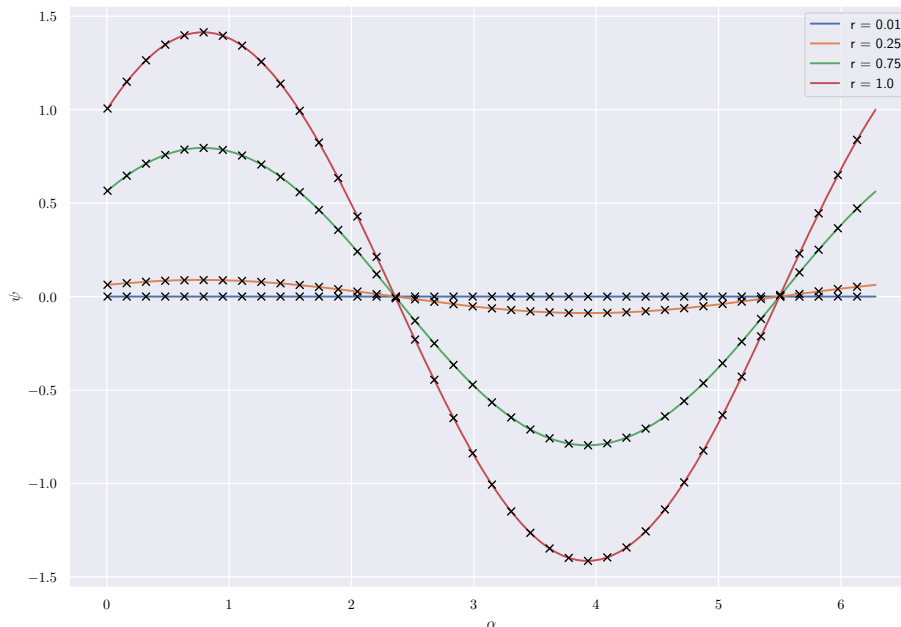


Fig. 7 Test solution of $\phi = r^2(\sin \theta + \cos \theta)$. Solid lines of various colours indicate the real solutions for different values of r of the unity circle; the black cross markers indicate the corresponding numerical solutions. The mean absolute error of the (1000×100) solution points is 5.578×10^{-6} , with $dr = 1.0 \times 10^{-2}$, $d\theta = 6.283 \times 10^{-3}$

6.1 Case 1

In the first case, the body resembles an inverted cone whose shape is given by $f = x^2 + (y/q)^2 - 1 + x\theta_1$, that is $g(x, y) = x^2 + (y/q)^2 - 1$. See Fig. 8b for a surface profile plot where q is taken to be unity, that is the body has the same length span in the x and y dimensions.

The fluid flows in the direction of the positive x -axis and slows down as it comes in contact with the body's leading surface. This is associated with an increase in flow pressure in a region at the body's leading edge; Fig. 8a shows the pressure of the fluid and Fig. 8b depicts such pressure exerted on the body surface in the form of a heat map. Past this leading contact region the flow increases in speed as the flow channel narrows, the speed reaches a maximum at the tip of the cone where the channel is at its narrowest. Such an increase in flow speed is marked by a drop in fluid pressure which is visualised by the heat map: a negative pressure region can be seen surrounding the tip of the cone and extending to the body's trailing edge, where the atmospheric pressure condition applies.

Figure 8c and d contrasts the fluid pressure for a body with narrow frontal profile facing the oncoming flow ($q = 0.1$) against one with a wide profile ($q = 10$), as can be seen by the different scales of the y -axis in the two figures. The fluid pressure for a flow past a body with a narrow frontal profile is comparatively small in magnitude and has less variation throughout the flow channel, but, on the other hand, the flow past a body with wide contact profile causes a large pressure variation. It is also interesting to note that a body with narrow profile where $q = 0.1$ has approximately 13% of its body surface subject to a positive pressure force, whereas for a wide profile case $q = 10$ less than 1% of its body surface experiences positive pressure lift.

Figure 9 shows the lift and torque forces exerted on the body for a range of span parameter q values (from 0.1 to 10). The body experiences a net suction as well as negative torque in all cases. The suction force on the body grows larger as the body increases in span q , while the torque force has two distinct behaviours: for a narrow body where $0 < q < 1$ it experiences an increasingly larger torque about the y -axis as q increases; for a wide body where $q \geq 1$ on the other hand, the torque gradually decreases as the body's span becomes wider.

Figure 10 demonstrates the evolution of the body's position over time where q is taken to be unity. Figure 10a shows the change of the pitch angle against the oncoming stream and the body's vertical centre of mass (CoM) position over time: the vertical CoM initially drops lower from its starting position due to the suction effect of the large negative pressure region under the body, but over time the net force under the body becomes positive as the region of positive pressure grows from the leading edge, which begins to lift the body upwards; the pitch

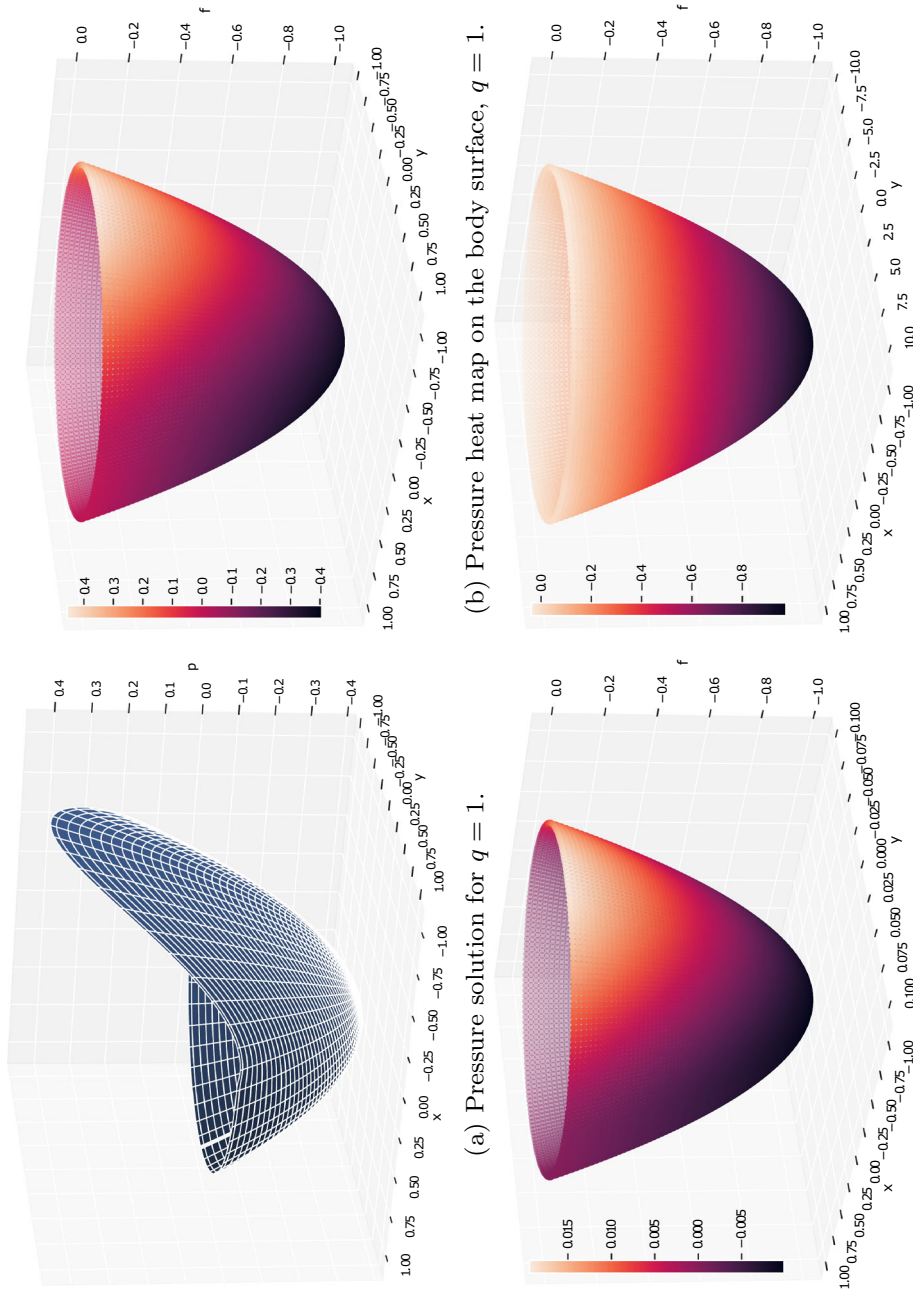


Fig. 8 Pressure plots of a body whose lower surface function is given as $f = x^2 + (y/q)^2 - 1 + x\theta_1$ for various values of q , with $\theta_1 = 0$

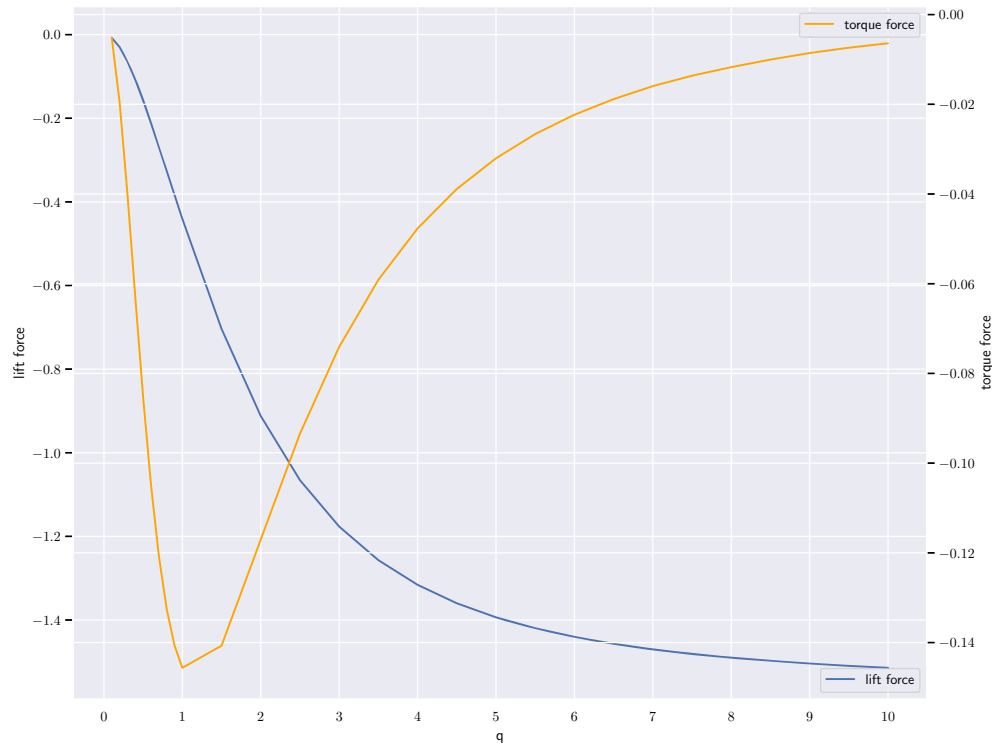


Fig. 9 Solutions of the lift and torque forces for a body with shape of $f = x^2 + (y/q)^2 - 1$ for different values of span parameter q . As the body increases in span ($q = 0.1, \dots, 10$), the negative pressure force under the body becomes more pronounced (blue line, left vertical axis). The torque force exerted on the body has two distinct behaviours (orange line, right axis): a body with narrow frontal contact profile $q < 1$ experiences a growing negative torque as q increases; for q becomes greater than one the torque on the body becomes smaller as q increases (colour figure online)

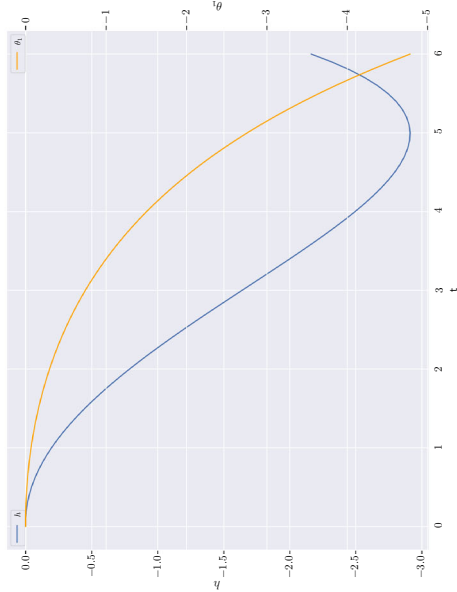
angle on the other hand becomes more negatively acute over time due to the torque resulting from the pressure distribution acting on the body surface. Figure 10b shows pressure profile under the body at simulation end time ($t = 6$): over time the positive pressure region grows in size as well as magnitude near the leading edge, which contributes to the net positive lift on the body as well as a negative torque about the y -axis.

6.2 Case 2

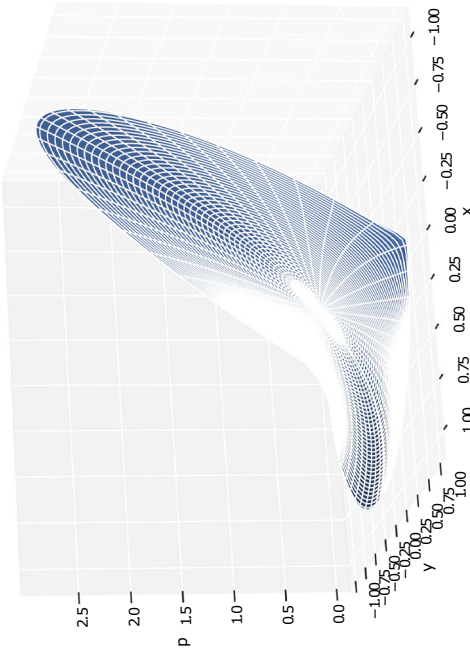
In our second case, the body shape is given by $f = \cos(\pi x/4) \cos(\pi y/(2q)) + x\theta_1$ and loosely resembles the chassis of an automobile or the under-carriage of a catamaran, as seen in Fig. 11b surface plot where q is taken to be unity.

The interactive behaviour for the present relatively complicated shape of case 2 and for the shape in case 1 can be explained in terms similar to those for the earlier more basic shapes. The fluid flows through a (vertically narrow) channel entrance at the leading edge into a wide-open region under the mid-section of the body; in contrast to the inverted cone case, the fluid first increases in speed as it flows past this leading edge and then slows down at the wide mid channel section, this flow behaviour being marked by a low pressure region near the body's leading edge and a correspondingly high pressure region in its mid flow section, where the body's surface height is at its greatest. As the flow approaches the trailing edge it increases in speed once again and the fluid pressure gradually drops to be atmospheric at this edge. See Fig. 11a for a 3D plot of the pressure solution and Fig. 11b for the corresponding pressure heat map on the body.

Figure 11c and d contrasts the fluid pressure for a body with narrow frontal profile facing the oncoming flow ($q = 0.1$) against one with a wide profile ($q = 10$). Consistent with the previous case study, the fluid pressure for a flow past a body with a narrow frontal profile is comparatively small in magnitude and has less variation throughout the flow channel, whereas the flow past a body with wide span has a comparatively greater pressure variation. We also note that a body with narrow profile where $q = 0.1$ has approximately 13% of its



(a) Evolution of body position over time.



(b) Pressure solution at time $t = 5$ where $\theta_1 \approx -4.78$.

Fig. 10 Evolution over time for body $f = x^2 + y^2 - 1 + x\theta_1$, ($q = 1$)

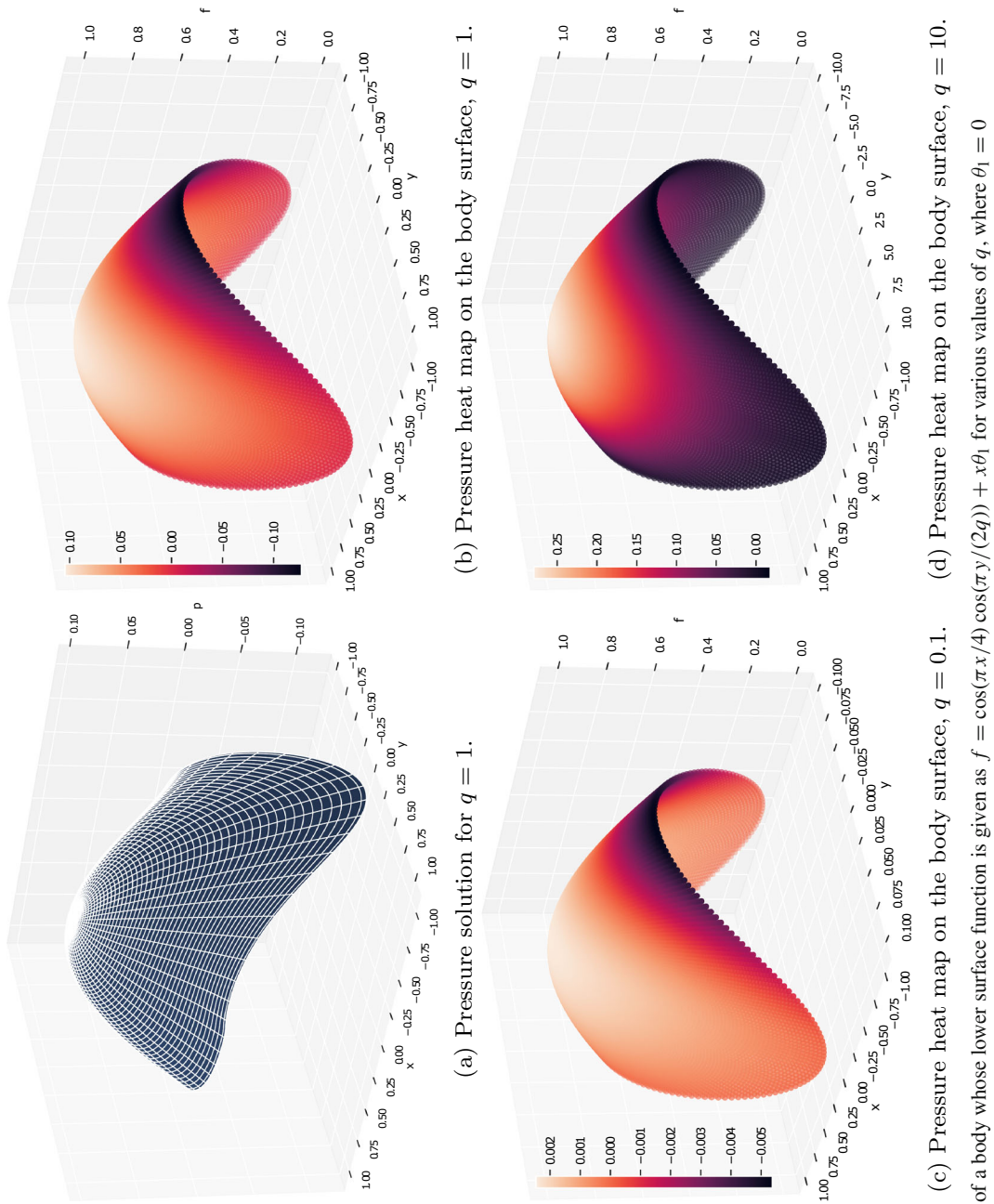


Fig. 11 Pressure plots of a body whose lower surface function is given as $f = \cos(\pi x/4) \cos(\pi y/(2q)) + x\theta_1$ for various values of q , where $\theta_1 = 0$

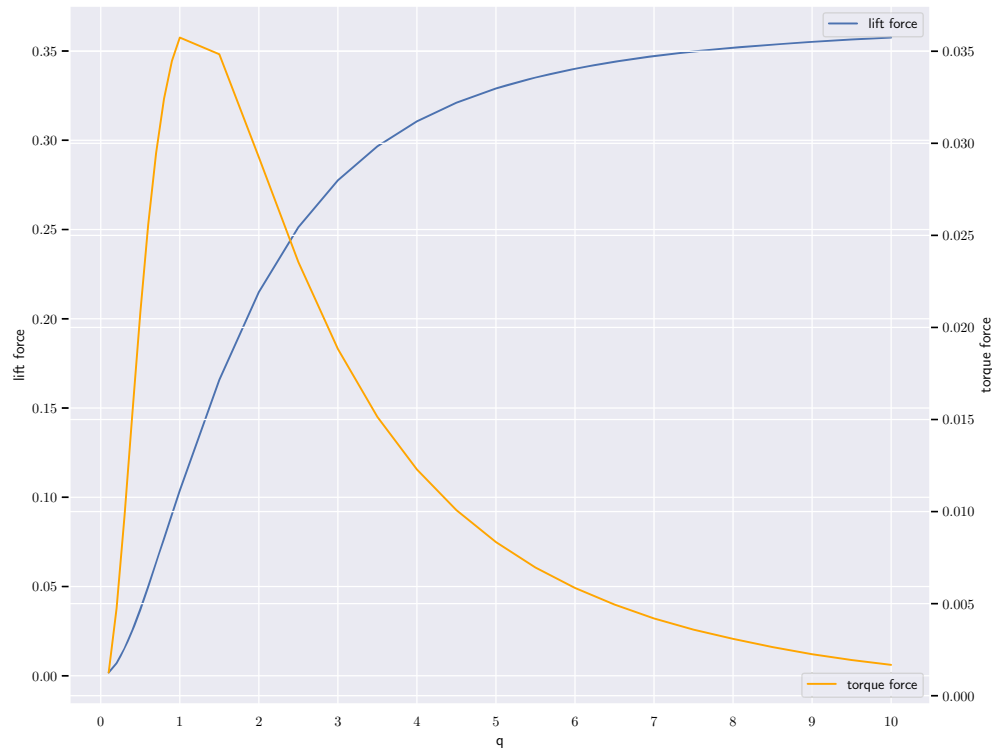


Fig. 12 Solutions of the lift and torque forces for a body with shape of $f = \cos(\pi x/4) \cos(\pi y/(2q))$ for different values of span parameter q . As the body increases in span ($q = 0.1, \dots, 10$), the positive pressure force under the body becomes more pronounced (blue line, left vertical axis). The torque force exerted on the body has two distinct behaviours (orange line, right axis): a body with narrow frontal contact profile $q < 1$ experiences a growing positive torque as q increases; for q becomes greater than one the torque on the body becomes smaller as q increases (colour figure online)

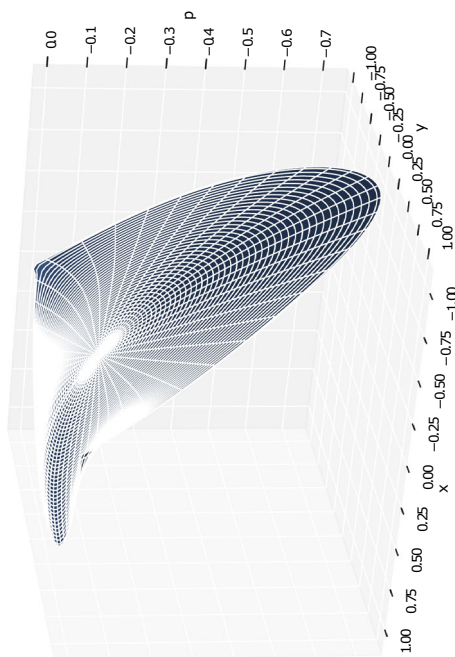
body surface near the leading edge subject to a negative pressure force, whereas for a wide profile case $q = 10$ less than 1% of its leading surface region experiences a negative pressure force.

Figure 12 shows the effect of the span parameter q on the lift and torque forces exerted on the body. We first note that the body experiences a net positive pressure force for all configurations of span (q ranges from 0.1 to 10), this contrasting with the case of an inverted cone where a net suction force is produced by the flow, thus reinforcing the importance of the surface shape in controlling pressure force effects. The suction force on the body grows larger as the body increases in span q , while the torque force has two distinct behaviours: for a narrow body where $0 < q < 1$ it experiences an increasingly larger torque about the y -axis as q increases; for a wide body where $q \geq 1$ on the other hand, the torque gradually decreases as the body's span becomes wider.

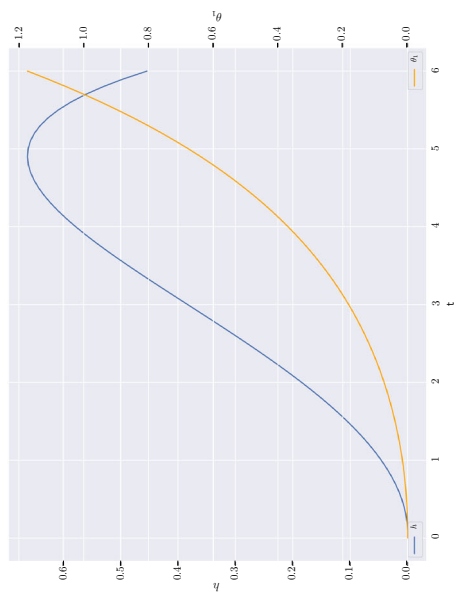
Figure 13 demonstrates the evolution of the body's position over time where q is taken to be unity. Figure 13a shows changes in the body's pitch angle against the oncoming stream and its vertical centre of mass (CoM) position: its vertical CoM initially climbs higher from its starting position due to positive pressure lift under the body, but as the pitch angle evolves this pressure force drops to below zero as the region of negative pressure grows from the leading edge. As a consequence, the body's vertical CoM drops lower; its pitch angle on the other hand becomes more positive over time due to the torque from the pressure distribution. Figure 13b shows pressure profile under the body at the simulation end time ($t = 6$): over time the negative pressure region grows in size as well as magnitude near the leading edge, which contributes to the gradual reduction in lift on the body as well as a positive torque about the y -axis.

7 Further discussion and conclusions

This study which has addressed numerically and analytically the evolution of three-dimensional body motion within, and interacting with, surrounding three-dimensional fluid motion is felt to have revealed some interesting features of fluid-body interaction. The unsteady interaction problem here is set near a solid wall and



(b) Pressure solution at time $t = 6$.



(a) Evolution of body position over time.

Fig. 13 Evolution over time for body $f = \cos(\pi x/4) \cos(\pi y/2) + x\theta_1$, ($g = 1$)

supposes the body to be solid and the fluid to be inviscid; flow separation is assumed to be absent. As regards the main findings, a dependence predominantly on the normal and pitch motions of the body has been shown in the formulation of Sects. 2 (nonlinear) and 3 (linearised), while instability or bounded oscillations are found from Sects. 4, 5 to depend on the position of the centre of mass of the body. The issue of instability or oscillations here is associated broadly with exponential growth of the normal and pitch deviations in which the underbody shape becomes negligible. Various cases of three-dimensional shapes have also been considered.

There is a useful comparison to be made between the present three-dimensional findings and those for two-dimensional interactions addressed in previous works. Foremost among these is probably the effect of moving the centre of mass of the body forward towards the leading edge. When the body is two-dimensional, or has a relatively wide span as discussed in Sect. 5, then the positioning x_c of the centre of mass has a critical value at the 1/3 chord station. If x_c is positioned ahead of this station then the fluid–body interaction tends to be stable, inducing oscillations, whereas an x_c value greater than 1/3 gives instability corresponding to exponential growth of small disturbances. By contrast, when the body is “very” three-dimensional, having a narrow span, then the critical positioning is at the 1/6 station, with stability (instability) being present upstream (downstream) of the critical value. The stabilising effect here is physically sensible. Another notable feature is that more variations in the underbody pressure responses arise in the three-dimensional interactive results.

A number of aspects that follow on from the present first study of unsteady three-dimensional interplay between a body and the surrounding fluid are equally interesting. First, the nonlinear version of the interactive system as originally formulated in Sect. 2 would be of considerable value. The roll motion of the body represented by variations in the angle θ_2 is then expected to come into play. Next, allowance could be made for an incident stream which is angled, with constant velocity components $U = Uw$, $W = Ww$ instead of the incoming stream in (4c). This yields a situation not dissimilar to that considered by Jones & Smith (2003) and a similar mathematical approach can be expected to hold. Third, the centre of mass positions x_c , y_c might vary, travelling at constant nonzero speed, and there may be a rotation of the body planform, as for a thrown discus or Frisbee, implying that the underbody shape can rotate. Finally here, other cases of dynamic fluid–body interaction such as in boundary layers and channel flows (Smith and Ellis [20], Smith and Wilson [21], Palmer and Smith [16], Jolley et al. [9]) would seem to call for spatially three-dimensional investigations. Although rather little progress has been seen previously, we believe there are many intriguing facets to explore in the future within this area of three-dimensional freely moving objects.

Open Access This article is licensed under a Creative Commons Attribution 4.0 International License, which permits use, sharing, adaptation, distribution and reproduction in any medium or format, as long as you give appropriate credit to the original author(s) and the source, provide a link to the Creative Commons licence, and indicate if changes were made. The images or other third party material in this article are included in the article’s Creative Commons licence, unless indicated otherwise in a credit line to the material. If material is not included in the article’s Creative Commons licence and your intended use is not permitted by statutory regulation or exceeds the permitted use, you will need to obtain permission directly from the copyright holder. To view a copy of this licence, visit <http://creativecommons.org/licenses/by/4.0/>.

Data availability The datasets generated during and/or analysed during the current study are available from the corresponding author on reasonable request.

Appendix: Analytical solution of a body with circular planform

This is the special case where $f = \theta_1 x$ whose visual illustration is given in Fig. 4a. The basic problem in the real plane is then to solve the Poisson equation

$$\Delta\phi = -\theta_1 \quad (39)$$

inside the semi-circle bounded by $r = 1$ and $y = 0$, together with the boundary conditions This corresponds to the special case where $f = \theta_1 x$ (which is also concerned with exponential growth, see below), whose visual illustration is given in Fig. 4a. The basic problem in the real plane is then to solve the Poisson equation

$$\Delta\phi = -\theta_1 \quad (40a)$$

inside the semi-circle bounded by $r = 1$ and $y = 0$, together with the boundary conditions given in (19).

In this subsection, we are working for convenience in terms of $x = r \cos \theta, y = r \sin \theta$ as the planar Cartesian coordinates and $\omega = x + iy$ is the associated complex coordinate. The condition (19c) stems from symmetry about the x -axis in the original circle case.

$$\phi = 0, \quad \left(at r = 1, \frac{\pi}{2} < \theta < \pi \right), \tag{40b}$$

$$\frac{\partial \phi}{\partial x} = 0, \quad \left(at r = 1, 0 < \theta < \frac{\pi}{2} \right), \tag{40c}$$

$$\frac{\partial \phi}{\partial y} = 0, \quad \left(at y = 0, -1 < x < 1 \right). \tag{40d}$$

In this subsection, we are working for convenience in terms of $x = r \cos \theta, y = r \sin \theta$ as the planar Cartesian coordinates and $\omega = x + iy$ is the associated complex coordinate.

First, we put $\phi/\theta_1 = -\frac{1}{2}y^2 + \hat{\phi}$, which transforms the problem to Laplace’s equation

$$\Delta \hat{\phi} = 0 \tag{41}$$

inside the semi-circle bounded by $r = 1$ and $y = 0$, with the boundary conditions becoming

$$\hat{\phi} = \frac{1}{2} \sin^2 \theta, \quad \left(at r = 1, \frac{\pi}{2} < \theta < \pi \right), \tag{42a}$$

$$\frac{\partial \hat{\phi}}{\partial x} = 0, \quad \left(at r = 1, 0 < \theta < \frac{\pi}{2} \right), \tag{42b}$$

$$\frac{\partial \hat{\phi}}{\partial y} = 0, \quad \left(at y = 0, -1 < x < 1 \right). \tag{42c}$$

Second, we apply a mapping of the interior of the semi-circle in the ω -plane to an upper half-plane in $\zeta = \xi + i\eta$ by means of the relation

$$\zeta = -\frac{1}{2} \left(\omega + \frac{1}{\omega} \right). \tag{43}$$

This maps the points ABC $(1, i, -1)$ lying on the boundary in ω to the points A'B'C' $(-1, 0, 1)$ lying along the ξ -axis in ζ , while the x -axis between -1 and 1 in the ω -plane is mapped to the two parts $\xi > 1, \xi < -1$ of the ξ - axis. See Fig. 14. In component form, the mapping reads as

$$\xi = -\frac{1}{2} \left(x + \frac{x}{x^2 + y^2} \right), \quad \eta = -\frac{1}{2} \left(y - \frac{y}{x^2 + y^2} \right), \tag{44a}$$

$$\xi = -\frac{1}{2} \left(r + \frac{1}{r} \right) \cos \theta, \quad \eta = -\frac{1}{2} \left(r - \frac{1}{r} \right) \sin \theta, \tag{44b}$$

thus confirming that inside the circle ($r < 1$) the ξ value can be positive or negative but η is positive.

Third, we consider the corresponding transformed problem which is to solve Laplace’s equation for $\hat{\phi}$ in terms of ξ, η (i.e. $\partial_\xi^2 \hat{\phi} + \partial_\eta^2 \hat{\phi} = 0$) within the upper half plane $\eta > 0$ subject to mixed boundary conditions along the ξ -axis and boundedness at infinity. Expressed in terms of the complex function

$$G_1(\zeta) = U_1 - iV_1 \tag{45}$$

where $U_1 = \partial \hat{\phi} / \partial \xi, V_1 = \partial \hat{\phi} / \partial \eta$, the conditions along the ξ -axis become

$$V_1 = 0, \quad (|\xi| > 1), \tag{46a}$$

$$U_1(\xi^2 - 1) + V_1 \xi(1 - \xi^2)^{\frac{1}{2}} = 0, \quad (-1 < \xi < 0), \tag{46b}$$

$$U_1 = -\xi, \quad (0 < \xi < 1). \tag{46c}$$

These confirm the crossover points as $\xi = -1, 0, 1$.

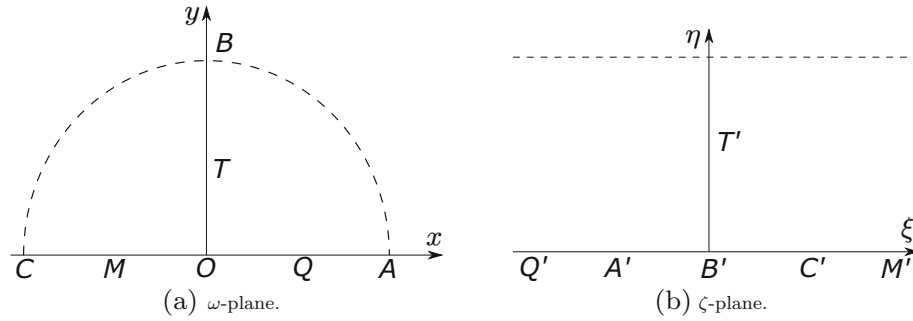


Fig. 14 Conformal mapping of the upper half circular flow domain for Laplace’s equation (41)

Fourth, we define the complex function

$$G_2(\zeta) = U_2 - iV_2 = (U_1 - iV_1)(\zeta - 1)^{\frac{1}{2}}(\zeta + 1)^{\frac{1}{2}} \tag{47}$$

in order to account for the main crossover points at $|\xi| = 1$. This is found to deal also with the crossover at $\xi = 0$. The square root functions are defined by $(\zeta - 1)^{\frac{1}{2}} = R_1 e^{i\beta_1}$, $(\eta + 1)^{\frac{1}{2}} = R_2 e^{i\beta_2}$ with angles β_1, β_2 between 0 and π in the upper half-plane. So along the ξ -axis, we have

$$U_2(\xi, 0) = \begin{cases} -U_1(\xi^2 - 1)^{\frac{1}{2}}, & (\xi < -1), \\ V_1(1 - \xi^2)^{\frac{1}{2}}, & (-1 < \xi < 0), \\ V_1(1 - \xi^2)^{\frac{1}{2}}, & (0 < \xi < 1), \\ U_1(\xi^2 - 1)^{\frac{1}{2}}, & (\xi > 1); \end{cases} \tag{48a}$$

$$V_2(\xi, 0) = \begin{cases} 0, & (\xi < -1), \\ -U_1(1 - \xi^2)^{\frac{1}{2}}, & (-1 < \xi < 0), \\ \xi(1 - \xi^2)^{\frac{1}{2}}, & (0 < \xi < 1), \\ 0, & (\xi > 1). \end{cases} \tag{48b}$$

We now use the Cauchy–Hilbert relation

$$U_2(\xi, 0) = \frac{1}{\pi} \int_{-\infty}^{\infty} \frac{V_2(s, 0)}{\xi - s} ds \tag{49}$$

which, applied for the interval $-1 < \xi < 0$ in particular and with the middle equation of (46) recalled, leads to the equation

$$\pi V_1(\xi, 0)(1 - \xi^2)^{\frac{1}{2}} = B(\xi) + P.V. \int_{-1}^0 \frac{s V_1(s, 0)}{\xi - s} ds. \tag{50}$$

Here, $B(\xi)$ is a known function,

$$B(\xi) = \int_0^1 \frac{s(1 - s^2)^{\frac{1}{2}}}{\xi - s} ds. \tag{51}$$

The singular integral equation (50) for $V_1(\xi, 0)$ applies for $-1 < \xi < 0$, with P.V. denoting the Cauchy principal value (Carrier et al. [2], pages 422-423).

We solved (50) for $V_1(\xi, 0)$ for $-1 < \xi < 0$ by means of an iterative scheme, and from the solution we also have $U_1(\xi, 0)$ there because of the middle equation of (46). Hence, we obtain $V_2(\xi, 0)$ for all ξ via (48b) and then $U_2(\xi, 0)$ follows for all ξ from (49). Finally, we can work back to deduce the scaled pressure $P = -\frac{\partial \hat{\phi}}{\partial x} = \xi(\xi^2 - 1) - \xi U_2(\xi, 0)$ for $0 < \xi < 1$, i.e. along “BC”, whose result is demonstrated in Fig. 4.

References

1. Sami Aköz, M., Salih Kırkgöz, M.: Numerical and experimental analyses of the flow around a horizontal wall-mounted circular cylinder. *Trans. Can. Soc. Mech. Eng.* **33**, 189–215 (2009)
2. Carrier, G.F., McCollough, C., Krook, M., Pearson, C.E., Pearson, K.E., Van Atta, L., Karreman Mathematics Research Collection.: *Functions of a Complex Variable: Theory and Technique*. McGraw-Hill (1966)
3. Maziar Dehghan and Hassan Basirat Tabrizi: Turbulence effects on the granular model of particle motion in a boundary layer flow. *Can. J. Chem. Eng.* **92**, 01 (2014)
4. Diplas, P., Dancy, C., Celik, A., Valyrakis, M., Greer, K., Akar, T.: The role of impulse on the initiation of particle movement under turbulent flow conditions. *Sci. (New York, N.Y.)* **11** **322**, 717–20 (2008)
5. Einav, S., Lee, S.L.: Particles migration in laminar boundary layer flow. *Int. J. Multiph. Flow* **1**(1), 73–88 (1973)
6. Foucaut, J.M., Stanislas, M.: Experimental study of saltating particle trajectories. *Exp. Fluids* **22**(4), 321–326 (1997)
7. Hall, G.R.: On the mechanics of transition produced by particles passing through an initially laminar boundary layer and the estimated effect on the lift performance of the x-21 aircraft (1964)
8. Hewitt, I., Balmforth, N., McElwaine, J.: Continual skipping on water. *J. Fluid Mech.* **669**, 328–353 (2011). <https://doi.org/10.1017/S0022112010005057>
9. Jolley, Ellen M., Palmer, Ryan A., Smith, Frank T.: Particle movement in a boundary layer. *J. Eng. Math.* **128**(1), 6 (2021)
10. Jones, M.A., Smith, F.T.: Fluid motion for car undertrays in ground effect. *J. Eng. Math.* **45**(3), 309–334 (2003)
11. Kudrolli, Arshad, Lumay, Geoffroy, Volfson, Dmitri, Tsimring, Lev S.: Swarming and swirling in self-propelled polar granular rods. *Phys. Rev. Lett.* **100**, 058001 (2008)
12. Arshad, K., David, S., Allen, B.: Critical shear rate and torque stability condition for a particle resting on a surface in a fluid flow. *J. Fluid Mech.* **808**, 397–409 (2016)
13. Loisel, V., Abbas, M., Masbernat, O., Climent, E.: The effect of neutrally buoyant finite-size particles on channel flows in the laminar-turbulent transition regime. *Phys. Fluids* **25**(12), 123304 (2013)
14. Miller, M.C., McCAYE, I.N., KOMAR, P. D.: Threshold of sediment motion under unidirectional currents. *Sedimentology* **24**(4), 507–527 (1977)
15. Owen, P.R.: Saltation of uniform grains in air. *J. Fluid Mech.* **20**(2), 225–242 (1964)
16. Palmer, Ryan A., Smith, Frank T.: A body in nonlinear near-wall shear flow: impacts, analysis and comparisons. *J. Fluid Mech.* **904**(A32), A32 (2020)
17. Petrie, H., Morris, P., Bajwa, A., Vincent, D.: Transition induced by fixed and freely convecting spherical particles in laminar boundary layers. Technical Report No. TR 93-07, The Penn State University Applied Research Laboratory (1993)
18. Portela, L., Cota, Pierpaolo, Oliemans, René: Numerical study of the near-wall behaviour of particles in turbulent pipe flows. *Powder Technol.* **125**, 149–157 (2002)
19. Schmidt, C., Young, T.: The impact of freely suspended particles on laminar boundary layers. 47th AIAA Aerospace Sciences Meeting including the New Horizons Forum and Aerospace Exposition. 10.2514/6.2009-1621 (2009)
20. Smith, F.T., Ellis, A.S.: On interaction between falling bodies and the surrounding fluid. *Mathematika* **56**(1), 140–168 (2010)
21. Smith, F.T., Wilson, P.L.: Body-rock or lift-off in flow. *J. Fluid Mech.* **735**, 91–119 (2013)
22. Virmavirta, M., Kivekäs, J., Komi, P.V.: Take-off aerodynamics in ski jumping. *J. Biomech.* **34**(4), 465–470 (2001)
23. Wang, J., Levy, E.K.: Particle behavior in the turbulent boundary layer of a dilute gas-particle flow past a flat plate. *Exp. Therm. Fluid Sci.* **30**(5), 473–483 (2006)